

A 450-day Light Curve of the Radio Afterglow of GRB 970508: Fireball Calorimetry

D. A. Frail¹, E. Waxman^{2,3}, & S. R. Kulkarni⁴

ABSTRACT

We report on the results of an extensive monitoring campaign of the radio afterglow of GRB 970508, lasting 450 days after the burst. The spectral and temporal radio behavior indicate that the fireball has undergone a transition to sub-relativistic expansion at $t \sim 100$ days. This allows us to perform “calorimetry” of the explosion. The derived total energy, $E_0 \sim 5 \times 10^{50}$ erg is well below the $\sim 5 \times 10^{51}$ erg inferred under the assumption of spherical symmetry from γ -ray and early afterglow observations. A natural consequence of this result, which can also account for deviations at $t < 100$ days from the spherical relativistic fireball model predictions, is that the fireball was initially a wide-angle jet of opening angle $\sim 30^\circ$.

Our analysis also allows to determine the energy fractions carried by electrons and magnetic field, and the density of ambient medium surrounding the fireball. We find that during the sub-relativistic expansion electrons and magnetic field are close to equipartition, and that the density of the ambient medium is $\sim 1 \text{ cm}^{-3}$. The inferred density rules out the possibility that the fireball expands into a strongly non-uniform medium, as would be expected, e.g., in the case of a massive star progenitor.

Subject headings: gamma rays: bursts – radio continuum: general

¹National Radio Astronomy Observatory, P. O. Box O, Socorro, NM 87801, USA

²Institute for Advanced Study, Princeton, NJ 08540, USA

³Department of Condensed-Matter Physics, Weizmann Institute, Rehovot 76100, Israel

⁴California Institute of Technology, Owens Valley Radio Observatory, 105-24, Pasadena, CA 91125, USA

1. Introduction

The gamma-ray burst (GRB) of May 8, 1997 was a watershed event in the study of these intriguing objects. There were two major advances resulting from afterglow observations of GRB 970508: (1) The first unambiguous evidence that some GRBs are a cosmological population was obtained with the detection of red-shifted metal lines in absorption against the optical afterglow (Metzger et al. 1997). The resulting lower limit on the distance, combined with the measured gamma-ray fluence, established an approximate energy scale for these events. (2) The discovery of the first radio afterglow and the demonstration of relativistic expansion of the fireball (Frail et al. 1997). The latter was made possible by the observations of distinctive variations in the radio flux and attributed to interstellar scintillation (Goodman 1997). It is worth noting that GRBs now join quasars and Galactic micro-quasars as sources for which superluminal motions have been inferred.

The afterglow from GRB 970508 was particularly bright and long-lived. Indeed, to this date, this GRB remains unusual in both these respects. Consequently, astronomers carried out intensive observations of the afterglow across the electromagnetic spectrum. The principal motivation of the observations were to infer the fundamental parameters of the explosion: the total energy of the explosion (E_0), the distribution of the circumburst medium (density, n_i and possible radial dependence as would be the case if the explosion took place in a circumburst medium shaped by mass loss from the progenitor) and the geometry of the afterglow (sphere versus collimated flow or “jets”).

Of all the parameters listed above, E_0 is perhaps the most eagerly sought parameter. After all, in a manner similar to supernovae, it is E_0 which sets the scale for the entire GRB phenomenon and thus it is a truly fundamental parameter of the explosion. With few exceptions (Katz & Piran 1997, Brainerd 1998) most of the early estimates for E_0 (Waxman 1997, Wijers & Galama 1999, Granot et al. 1999) lie within a factor of three of 10^{52} erg. Although their precise methodologies differ, all of these determinations use information gleaned from the early afterglow observations. Unfortunately, the Lorentz factor is large during the early phase and due to relativistic beaming the observer sees only solid angle Γ^{-2} of the emitting surface. Thus the inferred energy is necessarily the “isotropic equivalent” value. However, if fireballs are jet sources (as appears to be the case), such “isotropic equivalent” estimates are upper limits and in some cases can be gross upper limits (e.g. GRB 990510, Harrison et al. 1999).

Radio observations are essentially immune from the geometry of the fireball and thus offer us the best method to infer E_0 since much of the radio afterglow is emitted at later epoch when Γ is falling. Indeed, over the duration of the radio emission, the emitting material typically becomes sub-relativistic. Once the flow becomes sub-relativistic it will in due course also become spherical. Thus observations of radio afterglows allow us the opportunity of inferring E_0 without the usual concerns of the geometry of the fireball.

Radio observations offer two additional advantages: (1) At X-ray and optical wavelengths,

the afterglow emission rapidly enters the monotonic decaying regime within minutes to hours of the burst. Unfortunately, at the current time, logistical difficulties prevent us from responding so rapidly to GRB events. X-ray and optical afterglow observations are typically initiated hours after the burst. However, at radio wavelengths, the entire afterglow phenomenon is stretched in time. Thus monitoring the radio afterglow observations allows us to see all the important transitions (save the cooling transition) which in turn provides key diagnostics to infer the fundamental parameters of the explosion. (2) Radio observations offer us, via interstellar scintillations, the only way to measure the tiny angular size (few microarcseconds) of GRB afterglows. The measured size in turn allows us to verify the dynamics of the explosion.

In this paper, we present the complete radio light curves from the radio afterglow of GRB 970508 beginning 3.5 hrs after the burst and ending 450 d later when the source was no longer detectable. This is the third and final paper of an ambitious monitoring program that we initiated following the discovery of radio afterglow from GRB 970508. In the first paper (Frail et al. 1997) we reported the discovery of the radio afterglow and the first 90 d of observations, and we interpreted the strong variations as being due to diffractive scintillation. In the second paper (Waxman, Kulkarni & Frail 1998; hereafter, WKF98) we compared these observations to theoretical models and showed that the size estimated from diffractive scintillation was in excellent accord with that expected from hydrodynamical models. In the same paper we noted that the observed flux at late times ($t > 25$ d) was well below that predicted by a spherical model and suggested that this deviation was most likely explained by a jet-like geometry for the fireball rather than a sphere. We suggested that E_0 would be significantly lower than the 10^{52} erg isotropic equivalent estimate from the early afterglow observations and the isotropic equivalent γ -ray energy release and further suggested that the fireball would undergo a transition from relativistic to sub-relativistic expansion at $t \sim 100$ d.

The organization of the paper is as follows. The observations are summarized in §2. In §3 we present the basic results in the form of light curves in three bands, 8.46 GHz, 4.86 GHz and 1.43 GHz. In §4 we note a transition of the variations in the light curve from the diffractive to the refractive regimes. In §5 we compare the data to the expectations from the simple adiabatic fireball model. In §6 we point out important deviations from model predictions and argue that the afterglow was not spherical but was a jet with an opening angle of about 30 degrees. Finally, in §7 we propose a detailed sub-relativistic model which provides a satisfactory explanation to the very late time observations. The transition to non-relativistic regime allows us to carry out proper calorimetry of the explosion (§8).

2. Observations

Except where noted, all observations reported here were obtained at the Very Large Array (VLA) of the National Radio Astronomy Observatory (NRAO).⁵ The very first observation was made in the 1.4-GHz band, only 3.5 hrs after the initial gamma-ray detection of GRB 970508 (Costa et al. 1997). Table 1 lists each observing session giving the starting date, the time elapsed since the burst, the 1.43 GHz flux density of GRB 970508 ($F_{1.4} \pm \sigma_{1.4}$) and the VLA configuration. The first detection of the source was made on 1997 May 13.96 UT at 8.46 GHz. Except for the first week, it was customary to observe at 8.46 GHz and 4.86 GHz simultaneously, so we include them together in Table 2. All flux density measurements prior to 1997 August were previously compiled in Frail et al. (1997) but are listed here for completeness.

Calibration of the array phase was accomplished using extragalactic radio sources with well-known positions. J0410+769 was used primarily at 1.43 GHz while J0726+791 was the calibrator of choice for 4.86 GHz and 8.46 GHz. Since these compact sources usually vary on time scales of a month or more, the absolute flux scale (accurate to better than $\pm 2\%$) at each epoch for all frequencies was fixed with observations of 3C 48, 3C 147, and/or 3C 286.

The off-line analysis of the VLA data proceeded following standard practice using the AIPS data reduction package. When the radio afterglow from GRB 970508 was clearly detected, its flux density was measured by a Gaussian fitting procedure which solves for the peak and integrated intensity, the source position and its angular size. When the source is weak ($< 5\sigma$) and no reliable fit was possible, the peak flux density was measured from the image at the reported position of GRB 970508 (Taylor et al. 1997).

The error estimates in Tables 1 and 2 are based on the thermal noise fluctuations in the final image and are estimated by calculating the rms fluctuations in a region free of any obvious radio sources. In the D-array and to some extent in the CS array, where the resolution at 1.43 GHz is poor, the limiting sensitivity is not due to the receiver noise but to the contribution of unresolved, faint sources within the beam. This quantity varies from point to point in the sky but is of order $80 \mu\text{Jy}$ for a $45''$ beam at 1.4 GHz (Condon et al. 1998). Improperly cleaned sidelobes from the myriad sources in the D-array 1.43 GHz images constitute a further source of confusion. Together these effects can amount to $100 \mu\text{Jy}$ of uncertainty added in quadrature to the error estimates of the D-array measurements given in Table 1.

While the source confusion discussed above is negligible at 4.86 and 8.46 GHz, there is a second source of error in the largest array configurations (A and B) which can also be difficult to quantify. Atmospheric phase instabilities occurring on a time scale shorter than or comparable to the cycle time between calibrator and source will “scatter” flux from GRB 970508 and may introduce slight position offsets. Large and erratic excursions of the calibrator phase over the

⁵The NRAO is a facility of the National Science Foundation operated under cooperative agreement by Associated Universities, Inc.

course of an observing run are a useful diagnostic to indicate when this is occurring. Suspect data is revealed in off-line processing by sudden jumps in the flux density of the phase calibrator from its long-term average and a significant difference between the peak and integrated flux densities in the Gaussian fits of the radio emission from GRB 970508. Following these criteria it was necessary to discard data from only four epochs in 1997 (Sept. 19, Sept. 21, Dec. 23 and Dec. 26).

3. Results: Light Curves and Spectra

Late-Time Light Curves. In Figure 1 we show the entire light curve of all three frequencies at which GRB 970508 was monitored by the VLA. The behavior of the radio light curves in the first few months has been discussed elsewhere (Frail et al. 1997, WKF98); Galama et al. (1998a, b) and Shepherd et al. (1998) report a few additional points at low and high frequencies as well. For the sake of completeness, we now summarize the early time behavior here. As shown in Figure 2, the erratic flux variations reported in Frail et al. (1997) do not die away entirely after the first month but their character changes. Between 30 d and 85 d the 4.86 GHz and 8.46 GHz light curves have a mean flux density of $555 \pm 108 \mu\text{Jy}$ and $630 \pm 107 \mu\text{Jy}$, respectively. The modulation indices (defined as the ratio of the rms flux variations to the mean) are modest (15–20%) and the variations are well correlated between the two frequencies. This is very different from the narrow bandwidth, short time scale fluctuations seen in the first month and attributed to diffractive interstellar scattering (Frail et al. 1997). We return to this point in §4.

The light curve at 1.43 GHz (Table 1 and Figure 1) is markedly different than the other two. As noted elsewhere (Frail et al. 1997, Shepherd et al. 1998, Galama et al. 1998a) the 1.43 GHz flux density is initially weak ($125 \mu\text{Jy}$). This can best be understood if the source is optically thick at 1.43 GHz (Katz & Piran 1997). Near day 50 the source brightens considerably. Between 50 and 300 days its average flux density is $300 \mu\text{Jy}$ but with considerable scatter. Most of this scatter likely originates from source confusion, particularly in the more compact array configurations (see §2).

Near day 90 the light curves at 8.46 GHz and 4.86 GHz begin a power-law decay (Figure 3), similar to that which occurred much earlier at optical and X-ray wavelengths (Pian et al. 1998, Piro et al. 1998). Power-law fits to the light curves in Figure 3 for $t > 90$ d give values of $\alpha_{8.46} = -1.3 \pm 0.1$ and $\alpha_{4.86} = -1.1 \pm 0.1$ (defined as $f_\nu \propto t^\alpha$). The decline at 1.43 GHz is not as well constrained but we estimate from Figure 1 that the decay begins near day 300.

Spectral Index. Many of the features in the high frequency light curves have analogs in the spectral domain. For example, the narrow bandwidth ($\delta\nu \sim 4 \text{ GHz}$) diffractive scintillation seen by Frail et al. (1997) is best demonstrated in Figure 4 by the large swings in the spectral slope β (defined as $f_\nu \propto \nu^\beta$) between 8.46 GHz and 4.86 GHz. The spectral index appears to settle down by day 35 and we interpret this to mean that the diffractive scintillation has died down. Indeed, this is to be expected since only sources smaller than a critical size can undergo

diffractive scintillation. Thus at sufficiently late times, expansion will ensure that the source enters the refractive regime (§4). Since refractive scintillation is broadband (see §4) we see the true radio spectrum of the afterglow past day 35. Excluding two outlier points, the mean β for 11 measurements between day 40 and day 85 is $+0.25 \pm 0.04$ (Figure 4). Galama et al. (1998b) determined $\beta = 0.44 \pm 0.07$ near day 12. Since their estimate is based on extrapolations of the radio flux density when the source was scintillating strongly, the value of β given here should be a more accurate one.

In addition, the transition of the light curve to a power-law decay has a corresponding change in the spectral index plot of Figure 5, where β undergoes an abrupt drop from positive to negative values. The weighted mean β from day 95 to day 310 is -0.6 ± 0.3 . A joint fit to the spectrum and high frequency light curves of the form $f_\nu \propto t^\alpha \nu^\beta$ for $t > 110$ days yields more accurate values of $\beta = -0.50 \pm 0.06$ and $\alpha = -1.14 \pm 0.06$

Evolution of the Radio Spectrum. In Figure 6 we follow the evolution of the radio afterglow by plotting all radio frequencies at different time intervals. These spectral “snapshots” show that the spectrum initially rises with frequency, flattens and then finally exhibits a power-law slope which declines with frequency.

4. Refractive Scintillation

In Frail et al. (1997), we attributed the observed strong variability in the 8.46 GHz and 4.86 GHz bands over the course of the first month, to diffractive scintillation. The primary evidence for this inference is the observed strong, rapid (decorrelation time, $\delta t < 5$ hr) variability which is uncorrelated at 8.46 GHz and 4.86 GHz. These two characteristics, strong and chromatic variability, are the hallmarks of diffractive scintillation (Rickett 1977). In contrast, beyond day 30 the variations are not only milder but also correlated between the two frequencies (see §3). We attribute these variations to “refractive” scintillation.

Diffractive scintillation is caused by interference between rays diffracted by small-scale irregularities in the ionized interstellar medium. The resulting interference is narrow band and highly variable (with the modulation index approaching unity). Diffractive scintillation occurs only when the source size is smaller than a characteristic size, the so-called “diffractive” angle. Thus as the fireball expands we expect the diffractive scintillation to be quenched. However, as explained by Goodman (1997), focusing and defocusing of the wavefront by large scale inhomogeneities in the ionized interstellar medium will also result in scintillation, albeit at a reduced level on a longer time scale compared to diffractive variations. This “refractive” scintillation, unlike the earlier diffractive scintillation, is broad-band, and, most importantly, is much less sensitive to the size of the source. Thus, not surprisingly, refractive variability has been seen in many sources, whereas only the most compact sources – pulsars and GRB afterglows – show diffractive scintillation.

The light curves in Figure 1 and 2 show that the expected transition from the diffractive to

the refractive regime did take place. The flux variations decrease, but do not vanish, after the first month. During this period, the modulation index (defined as the ratio of the rms flux variations to the mean) is more modest (15–20%) compared to the first month when the modulation index was about 80%. The change in the nature of the flux variations is also seen in the spectral index curve (Figure 4). Over the first month, the flux variations were uncorrelated between 4.86 GHz and 8.46 GHz (decorrelation bandwidth, $\nu \leq 3$ GHz), as best demonstrated by the large swings in the spectral slope β whose values varied randomly between -1.2 to $+1.6$ from one day to the next (Figure 4). Starting around day 40, β converges to a constant value. We identify these slow, broad-band low-amplitude flux variations as being due to refractive scintillation, with the expansion of GRB 970508 taking it through a transition from the diffractive to refractive regimes.

In principle, an independent estimate of the angular size could be determined from the refractive scintillation, but our sampling of the light curve is not sufficient to accurately measure the refractive decorrelation time scale or the modulation index. Nonetheless, as a check for consistency, we now estimate the expected modulation index and refractive time scales and compare the same to the observations. We use the angular size of the fireball inferred from the diffractive scintillations, $\theta \sim 2 \mu\text{arcsec}$ at $t = 4$ weeks (WKF98), and extrapolate this size forward in time as $\theta \propto t^{5/8}$ to obtain a size of $3 \mu\text{arcsec}$ at $t = 8$ weeks. From this expected angular size, and using the formulation of Goodman (1997), we infer the refractive time scales to be between 10 and 20 hrs and the modulation indices of order 40% to 25% at these frequencies. These estimates are consistent with our admittedly meager data.

5. Comparison to Theory: A Relativistic Spherical Model

As remarked in §1 the principal motivation for afterglow observations is to deduce the fundamental parameters of the explosion. To this end, we now compare the radio observations with the expectation of the simplest model, the spherical adiabatic model. Other authors have carried out similar analyses but based only on early-time ($\lesssim 20$ d) multi-wavelength observations (Waxman 1997, Wijers & Galama 1999, Granot et al. 1999). They found good agreement with the basic expectation of spherical adiabatic models.

The first predictive afterglow models (Mészáros & Rees 1993, Paczyński & Rhoads 1993, Katz 1994, Mészáros & Rees 1997) actually preceded the discovery of the afterglow emission and have survived with relatively little modification (Sari 1997, Vietri 1997, Waxman 1997, Wijers, Rees & Mészáros 1997). In its most basic form the cosmological fireball model is a spherical blast wave, expanding adiabatically into a homogeneous medium of density n_i . A fixed fraction ϵ_e of the blast wave energy E_0 goes into accelerating a power-law distribution of electrons with energy slope p (where the number of electrons with Lorentz factor γ is $dn/d\gamma \propto \gamma^{-p}$ for $\gamma > \gamma_m$). In the presence of a magnetic field, which itself is a fixed fraction ϵ_B of the energy density of the blast wave, the electrons emit synchrotron radiation. The instantaneous synchrotron spectrum emitted by the electrons consists of four distinct spectral regimes and is given by Sari, Piran & Narayan

(1998) for the “slow cooling” case when the radiative cooling time for the majority of electrons with Lorentz factor $\gamma_e \sim \gamma_m$ is large compared to the dynamical time:

$$f_\nu \propto \begin{cases} \nu^2 t^{1/2} & \nu < \nu_{ab}, \\ \nu^{1/3} t^{1/2} & \nu_{ab} < \nu < \nu_m, \\ \nu^{-(p-1)/2} t^{-(3p-3)/4} & \nu_m < \nu < \nu_c, \\ \nu^{-p/2} t^{-(3p-2)/4} & \nu > \nu_c. \end{cases} \quad (1)$$

There are three transition frequencies: ν_{ab} , ν_m and ν_c . They correspond to (1) the synchrotron self-absorption frequency ν_{ab} below which the source becomes optically thick, (2) the peak frequency ν_m where the spectrum peaks at a flux density of F_{ν_m} and (3) the cooling frequency ν_c above which radiative losses steepen the observed spectrum. In time, as the blast wave interacts with the surrounding medium, the shape of the spectrum is preserved but the peak of the spectrum shifts to lower frequencies. The time-dependence of the three transition frequencies for an adiabatically expanding blast wave is given by $\nu_{ab} \propto t^0$, $\nu_m \propto t^{-3/2}$, and $\nu_c \propto t^{-1/2}$ with $\nu_{ab} < \nu_m < \nu_c$ for most of the time over which the afterglow is detectable. In addition, F_{ν_m} is expected to remain constant with frequency. Describing the evolution of the radio flux density as $F_R \propto t^\alpha \nu^\beta$ for $\nu_r > \nu_{ab}$ (i.e. the optically thin regime) we expect to see a slow rise to F_{ν_m} as $t^{1/2}$ for $\beta=+1/3$, followed by a power-law decline going as t^α , where $\alpha = 3\beta/2$ and $\beta = -(p-1)/2$ when $\nu_m \leq \nu_r$; and α steepening a further -0.25 when $\nu_c \leq \nu$.

The observations presented in §3 show substantially all of the gross spectral and temporal behavior expected from this basic model. In detail we find the following agreements with the model.

Low Energy Spectral Index. At early times synchrotron self-absorption is clearly detected (Figure 6 and Shepherd et al. 1998) with a synchrotron self-absorption frequency ν_{ab} near 3 GHz (Granot et al. 1999). After day 35 when the diffractive interstellar scintillation between 4.86 GHz and 8.46 GHz has quenched, the low energy regime of the synchrotron spectrum (i.e. $\nu_{ab} < \nu < \nu_m$) is revealed. The measured slope of $+0.25 \pm 0.04$ (Figure 5) is close to the predicted asymptotic value of $1/3$. This slope is a generic prediction of relativistic shocks which accelerate electrons with a power-law distribution of energies and have sharp cutoffs at low energies (Katz 1994).

Temporal Decay: Indices and Time scales. The decay in the 8.46 GHz and 4.86 GHz light curves (Figure 3) begins near day 90 and can be most easily seen in the spectral index plot of Figure 5, where the spectral slope undergoes an abrupt change from positive to negative values corresponding to the regime $\nu \geq \nu_m$. The corresponding light curves have a power-law decay with a temporal slope near -1.2 , comparable to that inferred from optical and X-ray observations (see Table 4).

As expected, the decay of the light curve for the lower frequency of 1.43 GHz begins much later (Figure 1). We can compare the time scale for the onset of the decay with the predicted

$t^{-3/2}$ dependence for ν_m . In Table 3 we give estimates of t_m between 1 and 100 GHz. The t_m from the 86 GHz data of Bremer et al. (1998) would predict that the onset of the power-law decay would start between 50–70 d at 8.46 GHz and between 70–95 d at 4.86 GHz. Similarly, from the 8.46 GHz and 4.86 GHz data we would predict a decay at 1.43 GHz between 200–300 d after the burst. Given the uncertainties in the estimates of t_m this agreement is surprisingly good.

Lack of cooling break. There is no evidence for the existence of an additional cooling break in the light curves or spectra of Figures 3 and 5. In contrast, Galama et al. (1998b,c) have identified passage of the cooling break at higher frequencies, specifically in the optical band around day 1.4. Accepting this result, the expected epoch of cooling break in the 8.46 GHz band is $t_c(O)(\nu_O/\nu_R)^2$, which is considerably larger than one year; here ν_O is the frequency in the optical band, $\sim 5 \times 10^{14}$ Hz, ν_R is the typical radio frequency and $t_c(O) \sim 1.4$ d. Thus, the absence of any clear cooling break in our radio light curves is not surprising.

6. Deviations From the Spherical Relativistic Model

In the previous section we found that the spherical adiabatic fireball model provided a satisfactory explanation for the observations at a gross level. However, on closer inspection there are several important differences between the radio afterglow of GRB 970508 and the model predictions. Indeed, on theoretical grounds we expect deviations from the spherical relativistic model due to a transition from relativistic to sub-relativistic regimes and possibly jet geometry (WKF98). We summarize the observed deviations below and offer explanations for them in §7.

Deviation in the Light Curves. As already noted in WKF98, the spherical model which provided an excellent fit to the early time (less than 3 weeks) multi-wavelength data (X-ray, optical and radio), predicted radio emission that was well above the observed value for $t > 25$ d; see Figure 1 of WKF98.

Non-constancy of Peak Flux. Another important prediction of the spherical, adiabatic model is the constancy of the peak flux density F_{ν_m} with time. While the peak frequency ν_m evolves as $t^{-3/2}$, the value of F_{ν_m} is expected to remain constant as ν_m sweeps through the X-ray, optical and radio bands. This assumption underlies all attempts to fit “snap-shot” broad-band spectral distribution of GRB afterglows (e.g. Galama et al. 1998b, Wijers & Galama 1999) and the subsequent derivation of the shock parameters. In Table 3 there is a very clear trend for successive peaks in F_{ν_m} to reach lower peak flux densities as ν_m moves towards lower frequencies. A least squares fit between 1 and 90 GHz gives $F_{\nu_m} \propto \nu_m^{0.40 \pm 0.04}$.

Non-constancy of Absorption Frequency. In the simple adiabatic fireball model, provided that the fundamental shock parameters (E_0 , n_i , ϵ_e and ϵ_B) do not change, ν_{ab} is expected to remain constant until such time as $\nu_m \leq \nu_{ab}$ (Waxman 1997, Granot et al. 1999). Near day 50 the 1.43 GHz flux density rises from ~ 125 μ Jy to ~ 300 μ Jy (see Figure 1). Such behavior is expected for an expanding optically thick source (see Frail et al. 1997) simply because of the increase in the

radiative surface area. However, the spectra in Figure 6 suggest a different interpretation. The initial attenuation at $t = 7$ d is well described by synchrotron self-absorption with unity optical depth at $\nu_{ab}=3$ GHz (Shepherd et al. 1998, Granot et al. 1999). In time, the spectra in Figure 6 clearly show an evolution from an optically thick to an optically thin source, with ν_{ab} shifting to lower frequencies.

Relation between α and β . The final and perhaps the most significant deviation from the model concerns the measured values for α and β (where $f_\nu \propto t^\alpha \nu^\beta$) of $\alpha = -1.14 \pm 0.06$ and $\beta = -0.50 \pm 0.06$ from the decay of the radio light curve. In Table 4 these values are compared to measurements made at optical wavelengths at different times in the evolution of the light curve. The temporal slope of the optical light steepens from its initial value of $\alpha = -0.9$ (Djorgovski et al. 1997) to -1.2 (e.g. Zharikov et al. 1998, Garcia et al. 1998, Castro-Tirado et al. 1998, Bloom et al. 1998). Similarly, the spectral slope undergoes an abrupt transition at optical wavelengths between day 1 and day 2 from $\beta = -0.6$ (Djorgovski et al. 1997) to $\beta = -1.1$ (Galama et al. 1998c, Sokolov et al. 1998). Galama et al (1998b) have made a strong case that this spectral and temporal break corresponded to the passage of the cooling break ν_c through the optical passbands at roughly 1.4 d after the burst. Prior to the passage of ν_c the relativistic model predicts $\alpha = 3\beta/2$, followed by a steepening (by 1/2) of β giving $\alpha = 3\beta/2 + 1/2$. The measured α and β on either side of ν_c values are consistent with these relationships. Bolstering this claim, Galama et al. (1998a) derived two independent measures of the electron energy power-law index ($p \simeq 2.2$). In contrast, in the framework of the relativistic adiabatic model, no single value of p can explain the values of α and β that we obtained from our radio observations. The radio α is identical to the late-time optical value but the radio β is more similar to the early optical estimates before ν_c moved through the optical band.

7. Jets and the Transition to the Sub-relativistic Regime

The relativistic spherical model is the simplest afterglow model and as such has received considerable attention from observers. Apart from the assumptions of constant ϵ_e , ϵ_B and acceleration to a power law spectrum, the main assumptions of the model are spherical geometry and relativistic outflow. Hints of deviations from the expectations of the spherical model were already apparent in the WKF98 paper (see 1).

In this section, we first qualitatively expand on these two ideas and find that the four problems identified in the previous section can be satisfactorily explained by a model incorporating jets. An inevitable consequence of a jet geometry is early (compared to spherical geometry) transition to the non-relativistic regime. We develop and present in Appendix A a formulation describing non-relativistic fireballs, and then apply this formulation to the light curves (Figure 1) and extract the basic parameters of the explosion in §8.

Deficit of Flux and Lack of Constancy of F_{ν_m} : Jets. A jet with an opening angle of θ_j

behaves as if it were a conical section of a spherical fireball, and cannot be distinguished by a distant observer from a spherical fireball, as long as the expansion Lorentz factor is larger than the inverse of the opening angle, $\gamma > \gamma_j \sim \theta_j^{-1}$. Once the jet decelerates to $\gamma < \gamma_j$, it expands sideways, leading to a decrease in blast wave energy per unit solid angle, which results in a deviation from spherical fireball behavior. The decrease in energy per unit solid angle leads to a decrease with time of F_{ν_m} , and suppresses the $t^{1/2}$ flux increase expected in the spherical model at frequencies $\nu < \nu_m$. Thus a jet geometry provides a reasonable explanation for the flattening of the radio light curves and the lack of constancy of F_{ν_m} (§6).

We set t_j , the epoch when the jet becomes apparent to the observer, as 25 d (see Figure 1 of WKF98; also discussion in §6). The Lorentz factor corresponding to this epoch is $\gamma_j \sim 2$, or equivalent to a jet opening angle $\theta_j \sim 30^\circ$. It was shown in WKF98 that on a time scale of $\gamma_j^2 t_j$, where t_j is the time at which the jet decelerates to $\gamma = \gamma_j$, the fireball approaches spherical, sub-relativistic expansion. A simple argument to understand this is as follows. The time at which we see deviation from spherical symmetry is $t_j \sim r_j/(2\gamma_j^2 c)$, where r_j is the radius at which $\gamma = \gamma_j \simeq \theta_j^{-1}$. The transition to spherical symmetry occurs over time scale $t_s \sim r_j/c$, i.e. $t_s \sim \gamma_j^2 t_j$. In addition, since the mass enclosed within a sphere of radius r_j , $M_j = 4\pi r_j^3 n_i m_p/3$, is comparable to the total jet energy $E_j \simeq E_{\text{sph.}}/2\gamma_j^2$, where $E_{\text{sph.}} = 16\pi r_j^3 \gamma_j^2 n m_p c^2/17$ is the energy inferred under the assumption of spherical symmetry, the fireball becomes sub-relativistic as it approaches spherical symmetry. Using our $t_j \sim 25$ d and $\gamma_j \sim 2$ we expect the fireball to approach spherical sub-relativistic expansion on a time scale of $t_s \sim 100$ d.

Relation between α and β : Sub-relativistic Fireball. As discussed in Appendix A, in the sub-relativistic regime, the afterglow emission scales as $f_\nu \propto t^\alpha \nu^\beta$ with $\beta = (p - 1)/2$ and $\alpha = 3\beta + 3/5$ (compared to $\alpha = 3\beta/2$ for relativistic expansion). The behavior of the radio flux observed at $t > 100$ d is consistent with this expectation since past day 100 (approximately the transition to sub-relativistic regime) we obtain $\alpha = -1.14 \pm 0.06$ and $\beta = -0.50 \pm 0.06$ (§3). If the afterglow was in the sub-relativistic regime, then we expect the following closure relation, $N = \alpha - 3\beta - 3/5 \equiv 0$, whereas in the relativistic regime, $R = \alpha - 3\beta/2 \equiv 0$. We find $N = -0.24 \pm 0.19$ whereas $R = -0.39 \pm 0.11$. Thus we can reject the relativistic model at the More importantly, a single value of $p=2.2$, explains, in a self-consistent way, the X-ray (Piro et al. 1998), optical (Galama et al. 1998b) and radio light (this paper) afterglow observations over several decades in time through radiative transitions (adiabatic to cooling) and dynamical transitions (relativistic to sub-relativistic).

Non-Constancy of ν_{ab} . The non-constancy of ν_{ab} can be explained as follows. There are two consequences in the sub-relativistic model when ν_m falls below ν_{ab} occurs (see WKF98 and Appendix A). First, ν_{ab} is no longer constant but evolves as $\propto t^{-2/3}$. Second, the peak in the spectrum is no longer at ν_m but is at ν_{ab} . The peak flux then evolves as $t^{-17/30}$. By itself, the observed decrease in ν_{ab} is consistent with the expectations of the sub-relativistic model. However, since one expects a similar temporal evolution of ν_{ab} for $\nu_m \leq \nu_{ab}$ in the relativistic model, it should not be taken as strong evidence in favor of the transition to sub-relativistic expansion.

The above conclusions, the manifestation of a jet at $t_j \sim 25$ d and the sub-relativistic transition at about epoch 100 d have been arrived at using extensive radio data presented in this paper. Independent support for this can be obtained from the optical data. As noted by Rhoads (1999) the optical data cannot be fitted by a single power law decay functional form. Rhoads derives a minimum beaming angle of $\theta_j = 30^\circ$, a value in complete agreement with our own. The principal strength of the radio result is the photometric uniformity of the data – the data were obtained with one instrument, the VLA, in a standard mode. In contrast, the optical data come from diverse sources and vexing cross-calibration issues still remain.

In our model, we would predict that the optical flux would steepen beyond t_j . A sharp break, such as the one seen in the light curve of GRB 990510 (e.g. Harrison et al. 1999), is not expected in the case of GRB 970508, given the wide opening angle. Numerical and analytical studies which track the dynamical evolution of the beamed ejecta (Moderski, Sikora, & Bulik 1999, Wei & Li 1999) find that unless the opening angle is very small or that lateral expansion is unimportant, a smooth and gradual transition is expected. In addition, past day 100, our model would predict a further, slight steepening [cf. Eq. (A20)] of the optical flux as the shock makes the transition from the relativistic to sub-relativistic regimes. The combination of these two factors is the likely origin for the apparent disappearance of the afterglow at $t \simeq 450$ d in a recent HST image (Fruchter et al. 1999).

8. Calorimetry of the Explosion

In Appendix A, we present a rigorous formulation of a sub-relativistic fireball model. In WKF98 we considered sub-relativistic fireball models in the asymptotic limit of ν_{ab} being very different from ν_m . However, for the data presented here, ν_m and ν_{ab} are comparable, and the model presented in Appendix A does not rely on asymptotic limits but is an exact model.

The radio flux and spectrum produced by the sub-relativistic fireball are determined by three parameters, a , b and ν_0 (see Appendix A). ν_0 is $(1+z)\nu_m$ at epoch t_0 . Here we set $t_0 = 100$ d and note that the redshift of the host galaxy of GRB 970508 is $z = 0.835$ (Bloom et al. 1998). The $t > 100$ d radio data allow an accurate ($\pm 10\%$) determination of the parameters a and b , which determine the high frequency flux normalization and the self-absorption suppression at 1.43 GHz: $a = 3.7 \times 10^{-51} \text{ g s}^{1/2}$, $b = 5.3 \times 10^{29} \text{ s}^{-3.1}$. The spectral change at $t \simeq 100$ d (Figure 5) implies that the peak frequency ν_m decreases through the frequency range of 8.46 GHz to 4.86 GHz at $t \simeq 100$ d, i.e. that $\nu_0/(1+z) \simeq 5$ GHz. However, it should be noted that since in our model the fireball at time $t = 100$ d is in transition to sub-relativistic spherical expansion (see below), significant deviation from the sub-relativistic model prediction is possible at $t = 100$ d. Thus, the determination of ν_0 is only approximate (see Figure 7). Our conclusions remain unchanged, however, even with a factor of a few change in ν_0 (see below).

The parameters a , b , and ν_0 are determined (see appendix A) by the four parameters, which

completely specify a sub-relativistic fireball model: the strength B_0 of the magnetic field at $t = t_0$, the minimum Lorentz factor γ_0 of the radiating electrons at $t = t_0$, the (time independent) number density n of the shocked plasma, and the shock radius r_0 at $t = t_0$. Using the three constraints provided by the determination of a , b and ν_0 we first derive B_0 , γ_0 , and n as functions of r_0 . We then constrain r_0 by requiring that the derived minimum energy of the radiating electrons and magnetic field does not exceed the thermal energy of the sub-relativistic fireball, given by the Sedov-von Neumann-Taylor formulation.

Using equation (A11) we find

$$B_0 = 5.2 \left(\frac{r_{18}}{d_*} \right)^4 a_*^{-2} \text{ G.} \quad (2)$$

We use the definitions $r_{18} = (r_0/10^{18} \text{ cm})$, $a = 4.1a_* \times 10^{-51} \text{ g s}^{1/2}$, $b = 5.3b_* \times 10^{29} \text{ s}^{-3.1}$, $\nu_0/(1+z) = 5.2\nu_* \text{ GHz}$, and $d = 0.94d_* \times 10^{28} \text{ cm}$. As demonstrated above, observations require $a_* = b_* = 1$, and $\nu_* \approx 1$. $d_* = 1$ for a flat universe with zero cosmological constant and $H_0 = 70 \text{ km s}^{-1} \text{ Mpc}^{-1}$. The minimum Lorentz factor is obtained from equation (A10),

$$\gamma_0 = 25.7\nu_*^{1/2} \left(\frac{r_{18}}{d_*} \right)^{-2} a_* \quad (3)$$

Finally, substitution of the above results into equation (A12) yields,

$$n = 0.005\eta_1\nu_*^{-0.6}b_*a_*^3r_{18}^{-7}d_*^6 \text{ cm}^{-3}, \quad (4)$$

where $\eta = 10\eta_1$; here r/η is the thickness of the shell of the fireball.

The ratio of electron to magnetic field energy densities is

$$\frac{E_e}{E_B} = \frac{p-1}{p-2} \frac{n\gamma_0 m_e c^2}{B^2/8\pi} = 5.4 \times 10^{-7} \eta_1 \nu_*^{-0.1} b_* a_*^8 r_{18}^{-17} d_*^{16}. \quad (5)$$

The minimum combined electron and magnetic field energy, $E_{min} = 1.92E_{ep}$ is obtained for a radius $r = r_{min} = 0.96r_{ep}$, where the equipartition radius r_{ep} is the radius for which $E_e = E_B = E_{ep}$. Using the above equations we obtain

$$r_{ep} = 4.3 \times 10^{17} \eta_1^{1/17} \nu_*^{-1/170} b_*^{1/17} a_*^{8/17} d_*^{16/17} \text{ cm,} \quad (6)$$

and

$$E_{min} = 2.3 \times 10^{50} \eta_1^{-6/17} \nu_*^{-11/170} b_*^{11/17} a_*^{20/17} d_*^{40/17} \text{ erg.} \quad (7)$$

During sub-relativistic expansion, the fireball hydrodynamics is described by the self-similar Sedov-von Neumann-Taylor solution. We now compare the equipartition energy with the energy of a Sedov-von Neumann-Taylor shock which reaches radius r_0 at time t_0 . This energy is given through the relation

$$r_0 = \xi(\hat{\gamma}) \left(\frac{E_{ST}}{n_i m_p} \right)^{1/5} \left(\frac{t_0}{1+z} \right)^{2/5}. \quad (8)$$

Here n_i is the ambient medium density, $\hat{\gamma}$ is the adiabatic index of the gas and ξ is close to unity for $\hat{\gamma}$ in the range of 4/3 (relativistic fluid) and 5/3 (non relativistic fluid). In what follows we use $\hat{\gamma} = 13/9$, appropriate for pressure equilibrium between relativistic electrons and non relativistic protons, for which $\xi(\hat{\gamma} = 4/3) = 1.05$. Using the above equations we have

$$E_{ST} = 4.4 \times 10^{50} \eta_1^{-2/17} \nu_{\star}^{-0.59} b_{\star}^{15/17} a_{\star}^{35/17} d_{\star}^{70/17} \left(\frac{r_0}{r_{ep}} \right)^{-2} \text{ erg.} \quad (9)$$

At $r = r_{ep}$ we find that the Sedov-Taylor energy is about twice the minimum electron and magnetic field energy required to account for the radio emission, $E_{ST}(r_0 = r_{ep}) \simeq 2E_{min}$.

The thermal energy in a Sedov-Taylor solution constitutes approximately half the total energy. The energy in the shocked electrons and in magnetic field clearly cannot exceed the thermal energy. Thus, we obtain an additional constraint, $E_{min} \leq E_{ST}/2$. As can be seen from the above equations this constraint can only be satisfied with $r_0 \sim r_{ep}$. For larger or smaller r_0 , $E_e + E_B$ would exceed the shock thermal energy, as $E_{ST} \propto (r_0/r_{ep})^{-2}$, while $E_e \propto (r_0/r_{ep})^{-6}$ and $E_B \propto (r_0/r_{ep})^{11}$.

Thus, although radio observations provide only three constraints on the four model parameters, a self-consistent solution is obtained only for

$$r_0 \simeq r_{ep} = 4.3 \times 10^{17} \eta_1^{1/17} \nu_{\star}^{-1/170} b_{\star}^{1/17} a_{\star}^{8/17} d_{\star}^{16/17} \text{ cm.} \quad (10)$$

This implies that electrons and magnetic fields are close to equipartition, that the fireball energy is

$$E \simeq E_{ST}(r_0 = r_{ep}) = 4.4 \times 10^{50} \eta_1^{-2/17} \nu_{\star}^{-0.59} b_{\star}^{15/17} a_{\star}^{35/17} d_{\star}^{70/17} \text{ erg,} \quad (11)$$

and that the ambient density is

$$n_i \simeq \frac{3}{\eta} n(r_0 = r_{ep}) = 0.53 \eta_1^{10/17} \nu_{\star}^{-0.56} b_{\star}^{10/17} a_{\star}^{-5/17} d_{\star}^{-10/17} \text{ cm}^{-3}. \quad (12)$$

Interstellar scintillations provide a direct and independent confirmation of the derived radius. As noted in WKF98, the observations of scintillation yield a fireball radius, $r \simeq 3 \times 10^{17}$ cm at $t = 25$ d which compares favorably with that stated in Equation 10. Furthermore, the shock radius derived in Equation (10) implies a shock velocity

$$\beta_{ST} \equiv \frac{2r}{5ct/(1+z)} = 0.6 \left(\frac{t}{300 \text{ d}} \right)^{-3/5}. \quad (13)$$

Thus, our model predicts relativistic to sub-relativistic transition at $t \sim 100$ d — as was indeed inferred from the $t < 100$ d data. We also note that, assuming jet expansion at $t \simeq 25$ d, the inferred fireball energy is $\lesssim 10^{51}$ erg, rather than the isotropic $\sim 10^{52}$ erg, and in excellent agreement with the value obtained using the $t > 100$ d data.

9. An Alternate Model

Based on these same radio data, Chevalier & Li (1999a) have proposed a model in which the afterglow is produced by the expansion of a shock into a circumburst medium, shaped by the mass loss history of the massive progenitor star. In this “wind” model, one expects the ambient density to be $\propto r^{-2}$ whereas the density is expected to be constant for an explosion in the typical interstellar medium. There is increasing support for such models, both in direct evidence linking supernovae with gamma-ray bursts (Galama et al. 1998d, Kulkarni et al. 1998), and indirect evidence in the optical and radio light curves of the afterglows (e.g. Bloom et al. 1999, Reichart 1999, Galama et al. 1999, Chevalier & Li 1999b, Frail et al. 1999).

The closure relation between α and β in the wind model can be expressed as $W = \alpha - 3\beta/2 + 1/2 \equiv 0$. This is consistent with our measured radio indices at $t > 100$ d, for which $W = 0.11 \pm 0.11$. However, the value of p would then be 1.85 which is unprecedented and energetically implausible. Moreover, the wind model of Chevalier & Li is not self-consistent. For their model parameters, the fireball expansion Lorentz factor is $\gamma=1.16$ at $t = 100$ d, from which we note that the expansion will become sub-relativistic for $t > 200$ d. Despite this, Chevalier & Li use extreme relativistic equations, valid only for $\gamma >> 1$, to compare their model predictions with data at $t > 100$ d (and ignore radio data at earlier times due to scintillation). In particular, the relation $W = \alpha - 3\beta/2 + 1/2 \equiv 0$ holds for $\gamma >> 1$ only.

We find the following additional inconsistencies in the Chevalier & Li wind model. First, at early time, $t \sim 1$ week their self-absorption frequency is $\nu_{ab} = 18(t/1\text{d})^{-3/5}$ GHz, which is in marked contradiction with the value inferred from the data, $\nu_{ab} \simeq 3$ GHz. Second, at late times they claim that optical flux is affected by cooling. However, there is an error in their Equation (62), and using their parameters for GRB 970508 with their Equation (9), one finds that $\nu_c = 0.8 \times 10^{14}(t/1\text{d})^{1/2}$ in their model, so that at $t = 100$ d the optical flux is not affected by cooling. As a result, the Chevalier & Li model gives an R-band flux at $t = 100$ d of $3\mu\text{Jy}$, an order of magnitude above what they claim to be their model prediction and inconsistent with the data. Finally, the wind model predicts an apparent fireball size of $r/\gamma = 0.8 \times 10^{18}$ cm at $t = 4$ weeks, an order of magnitude larger than the apparent size deduced from interstellar scintillations (WKF98).

10. Discussion and Conclusions

In this paper we present the 450-day radio afterglow curve of GRB 970508. This is by far the longest light curve obtained for any GRB. We also present a comprehensive model to explain the entire light curve. In our model, the fireball is a wide-angle jet which gradually expands sideways and becomes a spherical sub-relativistic shell by about day 100. The spherical symmetry of the fireball and the sub-relativistic expansion allow us to carry out calorimetry of the explosion, unhindered by unknown geometry. To our knowledge, this represents the first time that one has

been able to carry out absolute calorimetry of a GRB explosion. Below we summarize the salient features of the model and the principal results presented in this paper.

The comprehensive model we present has three regimes: (1) early afterglow, $2 < t < 25$ d, (2) jet afterglow, $25 < t < 100$ d and (3) spherical sub-relativistic afterglow. Several authors, in addition to us, have modeled the X-ray, optical and radio-afterglow observations of the early afterglow (e.g. Waxman 1997, Wijers & Galama 1999, Granot et al. 1999, WKF98). The modeling yield electron and magnetic field equipartition factors of $\epsilon_e \sim \epsilon_B \sim 0.1$. Estimates of the total explosion energy depend on the assumed fireball geometry (spherical versus jet). The high Lorentz factor hides the true geometry of the fireball. The inferred isotropic afterglow energy is $\sim 10^{52}$ erg which is comparable to the isotropic γ -ray energy release of 3.4×10^{51} erg.

The spherical model which explains the early afterglow quite nicely over-predicts the observed radio flux by day 25. We had earlier proposed that this discrepancy could be explained by invoking a jet geometry for the fireball (WKF98). To our knowledge this was the first explicit suggestion for a jet in a GRB.

We argue that the jet starts significant sideways expansion at $t \sim 25$ d, and that by day 100, the fireball becomes essentially a spherically symmetric sub-relativistically expanding shell. The primary observational evidence supporting the transition to the sub-relativistic regime is relation between power law temporal and spectral indices, which is inconsistent with relativistic expansion, and consistent with sub-relativistic expansion.

The radio observations presented here of the sub-relativistic phase of fireball expansion are unique. In this phase, the geometry of the fireball is no longer an issue, and the fireball dynamics is described by the well known Sedov-von Neumann-Taylor self-similar solution. Thanks to the extensive radio data (multi-band and long-term monitoring) we are able to deduce three out of the four fundamental parameters of the synchrotron emitting fireball shell: B_0 , the magnetic field strengths; n_i , the ambient density; r_0 , the radius of the shell; and γ_0 , the Lorentz factor of the emitting electrons. Leaving the radius as the free parameter we estimate the total energy of the emitting particles (including the energy in magnetic fields). We then use the constraint that this energy must not exceed the thermal energy of the a Sedov-von Neumann-Taylor expanding shell. This constraint then yields the size, and hence the total energy, of the expanding shell.

We find the following: $E_0 \sim 5 \times 10^{50}$ erg and $n_i \sim 0.5 \text{ cm}^{-3}$. Furthermore, we find that the electrons and magnetic field are close to equipartition with $\epsilon_e \sim \epsilon_B \sim 0.5$. Confidence in this “absolute” calorimetry is obtained when we note that the inferred size of the shell is comparable to that measured from interstellar scintillations (during the early phase). Furthermore, our model for $t > 100$ d predicts that the transition to sub-relativistic regime takes place at $t \sim 100$, as is indeed observed (see above).

Without any doubt, the most important result of this paper is the estimate of the total energy released in the explosion. This energy, $E_0 \sim 5 \times 10^{50}$ erg is well below 10^{52} erg, determined from early afterglow observations and the isotropic γ -ray energy release of 3.4×10^{51} erg. Thus the

energy release in GRB 970508 may not be much larger than that in ordinary SNe.

SRK and DAF are indebted to Barry Clark for his generous scheduling of the VLA for this long project. DAF thanks J. Katz and B. Paczyński for useful discussions. SRK’s research is supported by NSF and NASA. EW’s research is supported by AEC 38/99 and by BSF 9800343.

A. A Sub-Relativistic Model

A.1. Model assumptions

Since the fireball expands at a sub-relativistic velocity in our model, we assume to leading order that the radio flux observed at any given time is emitted by a static shell of radiating electrons. We denote the shell radius by r . During sub-relativistic expansion, the dynamics of the shell are described by the self-similar Sedov–von Neumann–Taylor solution. The shell radius and its velocity βc scale with time as

$$r = r_0(t/t_0)^{2/5}, \quad \beta = \beta_0(t/t_0)^{-3/5}. \quad (\text{A1})$$

Here t_0 is some (arbitrary) reference time, and the 0 subscripts denote parameter values at $t = t_0$. In what follows we use the normalization $t_0 = 100$ d. The compressed, shock heated, material behind the shock occupies a thin shell of width r/η , with $\eta \approx 10$. We assume that plasma parameters are uniform within the shell.

Electrons are assumed to be shock accelerated to a power-law energy distribution, $dn/d\gamma \propto \gamma^{-p}$ for $\gamma > \gamma_m$. We choose $p = 2.2$, as required by the high frequency observations. The magnetic field energy density, $B^2/8\pi$, and electron energy density, $(p-1)\gamma_m nm_e c^2/(p-2)$ are assumed to constitute fixed (time-independent) fractions of the shock thermal energy density. Under these assumptions, and recalling that the thermal energy density is proportional to β^2 , we have

$$B = B_0(t/t_0)^{-3/5}, \quad \gamma_m = \gamma_{m,0}(t/t_0)^{-6/5}. \quad (\text{A2})$$

A.2. Detailed spectrum

The synchrotron power per unit frequency ν emitted by a single electron of Lorentz factor γ is given by (Rybicki & Lightman 1979),

$$P(\nu, \gamma) = \frac{e^3 B}{m_e c^2} F \left[\frac{\nu}{\nu_c(B, \gamma)} \right], \quad (\text{A3})$$

where e and m_e are the electron charge and mass, and

$$\nu_c \equiv \gamma^2 \left(\frac{eB}{2\pi m_e c} \right). \quad (\text{A4})$$

The function $F(x)$ describes the synchrotron power spectrum (Rybicki & Lightman 1979), averaged over an isotropic distribution of pitch angles. To obtain the observed flux at a distance d one needs to integrate over the the angular distribution of the intensity I_ν at the surface of the shell, $f_\nu = 2\pi(r/d)^2 \int_0^1 d\cos\theta I_\nu(\theta) \cos\theta$. For a thin, $\eta \gg 1$, uniform shell, this integral is well approximated by

$$f_\nu = \left(\frac{1 - e^{-\tau_\nu}}{\tau_\nu} \right) 4\pi \left(\frac{r}{d} \right)^2 \frac{r}{\eta} j_\nu, \quad (\text{A5})$$

provided the effective optical depth is chosen as $\tau_\nu \equiv 4\alpha_\nu(r/\eta)$. Here j_ν is the synchrotron emissivity, $d = d_L(z)/(1+z)^{1/2}$, and α_ν is the synchrotron self-absorption coefficient.

For a power-law electron distribution we obtain

$$f_\nu = a(t/t_0)^{11/10} (1 - e^{-\tau_\nu}) [(1+z)\nu]^{5/2} f_3 \left(\frac{\nu}{\nu_m} \right) f_2^{-1} \left(\frac{\nu}{\nu_m} \right), \quad (\text{A6})$$

$$\tau_\nu \equiv b(t/t_0)^{1-(3p/2)} [(1+z)\nu]^{-(p+4)/2} f_2 \left(\frac{\nu}{\nu_m} \right). \quad (\text{A7})$$

Here

$$\nu_m \equiv \frac{\nu_c(\gamma = \gamma_m)}{1+z} = \frac{\nu_0}{1+z} (t/t_0)^{-3}, \quad (\text{A8})$$

the functions

$$f_l(x) \equiv \int_0^x dy F(y) y^{(p-l)/2}, \quad (\text{A9})$$

and the constants

$$\nu_0 \equiv \frac{1}{2\pi} \gamma_0^2 \frac{eB_0}{m_e c}, \quad (\text{A10})$$

$$a \equiv \frac{2\pi}{2+p} m_e \left(\frac{r_0}{d} \right)^2 \left(\frac{2\pi m_e c}{eB_0} \right)^{1/2}, \quad (\text{A11})$$

$$b \equiv \frac{(2+p)(p-1)}{4\pi\eta} \gamma_0^{p-1} n \left(\frac{e^3 B_0 r_0}{m_e^2 c^2} \right) \left(\frac{eB_0}{2\pi m_e c} \right)^{p/2}. \quad (\text{A12})$$

The model spectrum is determined by three parameters, a , b and ν_0 . These parameters, in turn, are determined by four model parameters, B_0 , r_0 , γ_0 and n .

A.3. Simple scalings

We define the self-absorption frequency ν_{ab} by $\tau_\nu(\nu = \nu_{ab}) = 1$. For $\nu_{ab} \ll \nu_m$, i.e. when the self-absorption frequency is much smaller than the characteristic synchrotron radiation frequency of the lowest energy electrons, f_ν peaks at $\nu_p \approx \nu_m$. The peak frequency and flux scale as

$$\nu_p \approx \nu_m \propto t^{-3}, \quad f_p \approx f_{\nu_m} \propto t^{3/5}, \quad (\text{A13})$$

and ν_{ab} scales as

$$\nu_{ab} \propto t^{6/5}. \quad (\text{A14})$$

The temporal and frequency dependence of f_ν is

$$f_\nu \propto \begin{cases} \nu^2 t^{-2/5} & \nu \ll \nu_{ab}, \\ \nu^{1/3} t^{8/5} & \nu_{ab} \ll \nu \ll \nu_m, \\ \nu^{-\beta} t^{-3\beta+(3/5)} & \nu_m \ll \nu, \end{cases} \quad (\text{A15})$$

where $\beta = (p - 1)/2$.

For $\nu_{ab} \gg \nu_m$, f_ν peaks at frequency $\nu_p \approx \nu_{ab}$. The optical depth at the peak frequency, $\tau_p \equiv \tau_\nu(\nu = \nu_p)$, satisfies

$$\frac{5}{p+4} (1 - e^{-\tau_p}) = \tau_p e^{-\tau_p}. \quad (\text{A16})$$

For $p = 2$ this implies $\tau_p = 0.35$, $\nu_p = 1.42\nu_{ab}$, and for $p = 3$ we have $\tau_p = 0.64$, $\nu_p = 1.14\nu_{ab}$. In this case,

$$\nu_p \approx \nu_{ab} \propto t^{-3(p-2/3)/(p+4)}, \quad f_p \propto t^{(3/5)-7(p-1)/(p+4)}, \quad (\text{A17})$$

and the temporal and frequency dependence of f_ν is

$$f_\nu \propto \begin{cases} \nu^2 t^{13/5} & \nu \ll \nu_m, \\ \nu^{5/2} t^{11/10} & \nu_m \ll \nu \ll \nu_{ab}, \\ \nu^{-\beta} t^{-3\beta+(3/5)} & \nu_{ab} \ll \nu. \end{cases} \quad (\text{A18})$$

In our analysis we have so far neglected the effects of synchrotron cooling of electrons. Synchrotron cooling is negligible for electrons radiating at radio frequencies, since $\nu_c \approx 5 \times 10^{13}$ Hz at $t = 100$ d (see §5), but may be important for electrons radiating at higher frequencies. The electron synchrotron cooling time is proportional to $1/\gamma B^2$, where γ is the electron Lorentz factor, while the shell expansion time is proportional to t . Thus, the Lorentz factor γ_c of electrons for which the cooling time is comparable to the expansion time scales as $\gamma_c \propto 1/B^2 t$, and the frequency ν_c , beyond which electron cooling affects the observed radiation, scales as

$$\nu_c \propto \gamma_c^2 B \propto B^{-3} t^{-2} \propto t^{-1/5}. \quad (\text{A19})$$

At frequencies higher than ν_c , electron cooling steepens the spectrum and

$$f_\nu \propto \nu^{-\beta-(1/2)} t^{-3\beta+(1/2)}, \quad \nu > \nu_c. \quad (\text{A20})$$

Note that for $p = 2$, $f_\nu \propto t^{-1}$ (at $\nu > \nu_c$) for both relativistic and sub-relativistic expansion.

REFERENCES

Bloom, J. S. et al. 1999, Nature, in press (astro-ph/9905301)

Bloom, J. S., Djorgovski, S. G., Kulkarni, S. R., & Frail, D. A. 1998, *Ap. J. (Letters)*, **507**, L25.

Brainerd, J. J. 1998, *Ap. J. (Letters)*, **496**, L67.

Bremer, M., Krichbaum, T. P., Galama, T. J., Castro-Tirado, A. J., Frontera, F., van Paradijs, J., Mirabel, I. F., & Costa, E. 1998, *A&A*, 332, L13.

Condon, J. J., Cotton, W. D., Greisen, E. W., Yin, Q. F., Perley, R. A., Taylor, G. B., & Broderick, J. J. 1998, *AJ*, 115, 1693.

Castro-Tirado, A. J. et al. 1998, *Science*, 279, 1011.

Chevalier, R. A. & Li, Z.-Y. 1999a, *ApJ* submitted (astro-ph/9908272)

Chevalier, R. A. & Li, Z.-Y. 1999b, *Ap. J. (Letters)*, **520**, L29.

Costa, E. et al. 1997, *IAU Circ.* No. 6649

Djorgovski, S. G., et al. 1997, *Nature*, **387**, 876.

Frail, D. A. et al. 1999, *ApJ(Let)* submitted

Frail, D. A., Kulkarni, S. R., Nicastro, L., Feroci, M., & Taylor, G. B. 1997, *Nature*, **389**, 261.

Fruchter, A. S. et al. 1999, astro-ph/9903236

Galama, T. J. et al. 1998a, *Ap. J. (Letters)*, **500**, 101.

Galama, T. J., Wijers, R. A. M. J., Bremer, M., Groot, P. J., Strom, R. G., Kouveliotou, C., & van Paradijs, J. 1998b, *Ap. J. (Letters)*, **500**, 97.

Galama, T. J. et al. 1998c, *Ap. J. (Letters)*, **497**, L13.

Galama, T. J. et al. 1998d, *Nature*, **395**, 670.

Garcia, M. R. et al. 1998, *Ap. J. (Letters)*, **500**, 105.

Goodman J. 1997, *New Astro.*, 2, 449

Granot, J., Piran, T., & Sari, R. 1999, *ApJ* in press (Dec 10 issue)

Harrison, F. A. et al. 1999, *Ap. J. (Letters)*, **523**, 121.

Katz, J. I. 1994, *Ap. J. (Letters)*, **432**, 107.

Katz, J. I., & Piran, T. 1997, *Ap. J.*, **490**, 772.

Mészáros, P. & Rees, M. J. 1993, *Ap. J.*, **405**, 278.

Mészáros, P. & Rees, M. J. 1997, *Ap. J.*, **476**, 232.

Metzger, M. R., Djorgovski, S. G., Kulkarni, S. R., Steidel, C. C., Adelberger, K. L., Frail, D. A., Costa, E., & Frontera, F. 1997, *Nature*, **387**, 879.

Moderski, R., Sikora, M., & Bulik, T. 1999, astro-ph/9904310

Paczyński, B. & Rhoads, J. E. 1993, *Ap. J. (Letters)*, **418**, L5.

Pian, E. et al. 1998, *Ap. J. (Letters)*, **492**, L103.

Piro, L. et al. 1998, *A&A*, 331, L41.

Pooley, G. & Green, D. 1997, IAU Circ. No. 6670

Reichart, D. E. 1999, *ApJ(Letters)* in press (astro-ph/9906079)

Rhoads, J. E. 1999, *A&A Sup.* in press (astro-ph/9903400)

Rickett, R. J. *ARAA*, 15, 479

Rybicki, G. B. & Lightman, A. P.: 1979, John Wiley & Sons, New York

Sari, R. 1997, *Ap. J. (Letters)*, **489**, L37.

Sari, R., Piran, T., & Narayan, R. 1998, *Ap. J. (Letters)*, **497**, L17.

Shepherd, D. S., Frail, D. A., Kulkarni, S. R., & Metzger, M. R. 1998, *Ap. J.*, **497**, 859.

Sokolov, V. V., Kopylov, A. I., Zharikov, S. V., Feroci, M., Nicastro, L., & Palazzi, E. 1998, *A&A*, 334, 117.

Taylor, G., Frail, D. A., Beasley, A. J., & Kulkarni, S. R. 1997, *Nature*, **389**, 263.

Vietri, M. 1997, *Ap. J. (Letters)*, **488**, L105.

Waxman, E. 1997, *Ap. J. (Letters)*, **489**, L33.

Waxman, E., Kulkarni, S. R., & Frail, D. A. 1998, *Ap. J.*, **497**, 288.

Wei, D. M., & Lu, T. 1999, astro-ph/9908273

Wijers, R. A. M. J., & Galama, T. J. 1999, *ApJ*, submitted (astro-ph/9805341).

Wijers, R. A. M. J., Rees, M. J., & Mészáros, P. 1997, *M.N.R.A.S.*, **288**, 51.

Zharikov, S. V., Sokolov, V. V., & Baryshev, Y. V. 1998, *A&A*, 337, 356.

Table 1. 1.43 GHz Observations of GRB 970508

Date (UT)	Δt (days)	$F_{1.4}^a$ (μ Jy)	$\sigma_{1.4}$ (μ Jy)	Array Config. ^b
1997 May 9.05	0.15	...	45	B
1997 May 9.84	0.93	...	89	B
1997 May 15.09	6.19	100	32	B
1997 May 18.83	9.93	...	63	B
1997 Jun. 1.00	23.10	...	52	CnB
1997 Jun. 2.32	24.41	135	45	CnB
1997 Jun. 12.83	34.93	130	20	CnB
1997 Jul. 18.62	70.72	305	48	C
1997 Jul. 28.94	81.03	485	45	CS
1997 Aug. 19.02	102.11	250	70	CS
1997 Aug. 22.52	105.62	230	59	CS
1997 Sep. 3.47	117.56	206	63	CS
1997 Sep. 8.42	122.51	216	67	CS
1997 Sep. 12.68	126.78	333	65	CS
1997 Sep. 26.35	140.45	...	83	DnC
1997 Oct. 4.63	148.73	217	105	DnC
1997 Oct. 13.22	157.32	381	127	DnC
1997 Oct. 21.39	165.48	250	66	DnC
1997 Nov. 8.09	183.19	338	63	D
1997 Nov. 11.33	186.42	497	51	D
1997 Nov. 13.97	189.06	376	93	D
1997 Nov. 17.65	192.75	...	93	D
1997 Nov. 19.46	194.55	303	53	D
1997 Nov. 22.46	197.56	199	62	D
1997 Nov. 23.05	198.14	271	74	D
1997 Nov. 24.96	200.05	208	77	D
1997 Nov. 26.17	201.26	155	43	D
1997 Nov. 27.12	202.21	170	50	D
1997 Nov. 28.40	203.50	...	62	D
1997 Nov. 30.32	205.42	184	42	D
1997 Dec. 1.40	206.49	...	71	D
1997 Dec. 6.65	211.75	...	68	D
1997 Dec. 11.16	216.25	...	64	D
1998 Feb. 23.44	290.53	274	27	A
1998 Mar. 18.06	313.16	434	24	A
1998 Apr. 27.66	353.76	249	60	A
1998 May 2.52	358.62	204	30	A
1998 Jul. 19.78	436.89	...	32	B
1998 Jul. 28.73	445.83	...	33	B

^aWhen no flux density measurement is given it can be assumed that the source was not detected above the $3\sigma_{1.4}$ level.

^bThe 27 antennas of the VLA can be placed into one of four “standard” configurations (A, B, C and D) giving a synthesized beamsize (i.e. resolution) of 1.2'' in A-array and increasing in multiples of 3.3 to the D-array resolution of 44''. Hybrid arrays such as DnC and CnB have increased resolution in the north-south direction, while the CS array is a special C-array hybrid designed for increased sensitivity to extended emission.

Table 2. 4.86 and 8.46 GHz Observations of GRB 970508

Date (UT)	Δt (days)	$F_{4.86}$ (μ Jy)	$\sigma_{4.86}$ (μ Jy)	$F_{8.46}$ (μ Jy)	$\sigma_{8.46}$ (μ Jy)	Array Config. ^a
1997 May 13.96	5.06	430	25	B
1997 May 15.13	6.23	330	33	610	33	B
1997 May 16.49	7.59	520	18	B
1997 May 16.79	7.89	602	24	V
1997 May 17.30	8.40	604	56	V
1997 May 18.85	9.95	480	64	610	51	B
1997 May 21.00	12.10	1270	120	V
1997 May 21.13	12.23	930	120	V
1997 May 22.10	13.20	410	47	570	42	B
1997 May 22.49	13.59	360	31	880	33	B
1997 May 23.00	14.10	1260	100	V
1997 May 23.13	14.23	960	100	V
1997 May 24.48	15.58	550	44	B
1997 May 24.96	16.06	470	43	B
1997 May 25.85	16.95	480	45	B
1997 May 27.67	18.77	770	54	500	49	B
1997 May 28.10	19.20	538	100	V
1997 May 28.23	19.33	835	100	V
1997 May 29.10	20.20	1350	55	1200	47	CnB
1997 May 30.95	22.05	740	46	810	48	CnB
1997 May 31.99	23.09	550	43	290	46	CnB
1997 Jun. 2.29	24.39	650	44	720	62	CnB
1997 Jun. 2.41	24.51	940	27	CnB
1997 Jun. 2.50	24.60	960	40	V
1997 Jun. 2.90	25.00	540	46	760	45	CnB
1997 Jun. 3.94	26.04	530	51	670	43	CnB
1997 Jun. 5.97	28.07	850	36	690	28	CnB
1997 Jun. 9.74	31.84	470	38	530	38	CnB
1997 Jun. 12.99	35.09	640	43	600	39	CnB
1997 Jun. 14.73	36.83	590	69	460	66	CnB
1997 Jun. 17.92	40.02	400	49	560	40	CnB
1997 Jun. 18.96	41.06	640	55	630	63	CnB
1997 Jun. 20.86	42.96	550	36	800	32	CnB
1997 Jun. 22.93	45.03	425	43	645	38	CnB
1997 Jun. 26.63	48.73	610	70	680	46	CnB
1997 Jun. 28.68	50.78	500	34	565	36	C
1997 Jul. 2.36	54.46	805	38	805	43	C
1997 Jul. 4.59	56.69	605	50	710	49	C
1997 Jul. 11.10	63.20	630	32	725	40	C
1997 Jul. 14.61	66.71	585	48	680	46	C
1997 Jul. 15.33	67.43	550	31	630	37	C
1997 Jul. 18.44	70.54	505	62	575	61	C
1997 Jul. 18.64	70.74	535	43	515	41	C
1997 Jul. 22.55	74.65	385	51	440	51	CS
1997 Jul. 30.46	82.56	360	70	455	85	CS
1997 Aug. 4.01	87.11	370	38	380	42	CS
1997 Aug. 5.35	88.45	550	61	445	50	CS
1997 Aug. 7.23	90.33	515	37	430	39	CS
1997 Aug. 11.26	94.36	615	37	640	40	CS
1997 Aug. 15.13	98.23	770	57	565	49	CS
1997 Aug. 16.62	99.72	610	55	400	60	CS
1997 Aug. 18.95	102.05	500	42	300	35	CS

Table 2—Continued

Date (UT)	Δt (days)	$F_{4.86}$ (μ Jy)	$\sigma_{4.86}$ (μ Jy)	$F_{8.46}$ (μ Jy)	$\sigma_{8.46}$ (μ Jy)	Array Config. ^a
1997 Aug. 22.50	105.60	710	52	470	44	CS
1997 Aug. 31.82	114.92	315	70	DnC
1997 Sep. 3.45	117.55	425	57	355	47	DnC
1997 Sep. 4.71	118.81	370	70	DnC
1997 Sep. 8.40	122.50	350	47	DnC
1997 Sep. 12.64	126.74	400	41	370	39	DnC
1997 Sep. 26.36	140.46	380	40	330	45	DnC
1997 Oct. 4.62	148.72	420	44	310	56	DnC
1997 Oct. 13.23	157.33	350	40	280	37	DnC
1997 Oct. 21.40	165.50	300	34	240	34	DnC
1997 Oct. 26.56	170.66	280	31	300	37	DnC
1997 Nov. 6.19	181.29	385	32	240	24	D
1997 Nov. 19.15	194.25	325	37	240	30	D
1997 Dec. 9.14	214.24	180	35	170	30	D
1998 Jan. 2.08	238.18	220	35	160	30	D
1998 Jan. 18.90	255.00	275	53	D
1998 Jan. 20.98	257.08	235	41	150	36	D
1998 Jan. 27.77	263.87	220	50	...	50	D
1998 Jan. 31.29	267.39	...	80	...	50	D
1998 Feb. 8.04	275.14	200	24	95	24	A
1998 Mar. 14.09	309.19	165	17	105	15	A
1998 May 13.52	369.62	125	28	...	25	A
1998 Jun. 21.83	408.93	104	44	...	37	BnA

^aLetter designations for the array configurations are explained in the table notes of Table 1. A “V” denotes flux density measurements obtained using the VLBA by Taylor et al. (1997).

Table 3. The Transition to the Power-Law Regime

ν_m (GHz)	t_m (days)	F_{ν_m} (μ Jy)	σ_{rms} (μ Jy)	References
86.2	10-14	1620	250	Bremer et al. (1998)
15.0	8-13	660	110	Pooley & Green (1997)
8.46	~90	630	107	this paper
4.86	~90	555	108	this paper
1.43	310-490	300	150	this paper

Table 4. Spectral and Temporal Power-Law Indices

Time Range (days)	α^a	β^a	References
2-4	-0.9 ± 0.1	-0.65 ± 0.3	Djorgovski et al. (1997)
2-25	-1.13 ± 0.04	-1	Pian et al. (1998)
2-120	-1.191 ± 0.024	-1.11 ± 0.06	Galama et al. (1998c)
2-90	-1.171 ± 0.012	-1.1	Sokolov et al. (1998)
2-100	-1.23 ± 0.04	-1.10 ± 0.08	Zharikov et al. (1998)
90-300	-1.14 ± 0.06	-0.50 ± 0.06	this paper

^aThe flux density $f_\nu \propto t^\alpha \nu^\beta$.

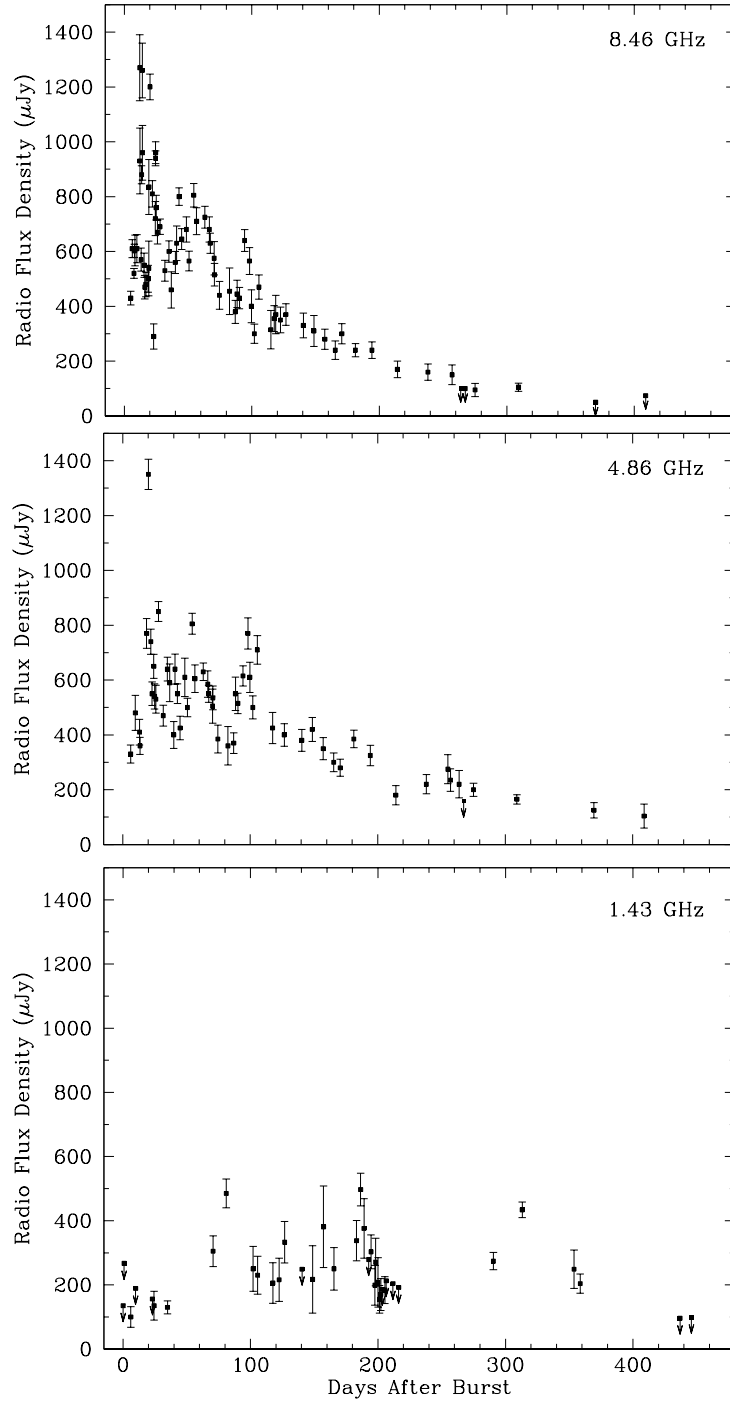


Fig. 1.— The radio light curves of GRB 970508 at 8.46, 4.86 and 1.43 GHz in their entirety. The data are taken from Tables 1 and 2. Upper limits are indicated by arrows, with 2σ limits plotted at 8.46 GHz and 4.86 GHz and 3σ limits plotted at 1.43 GHz.

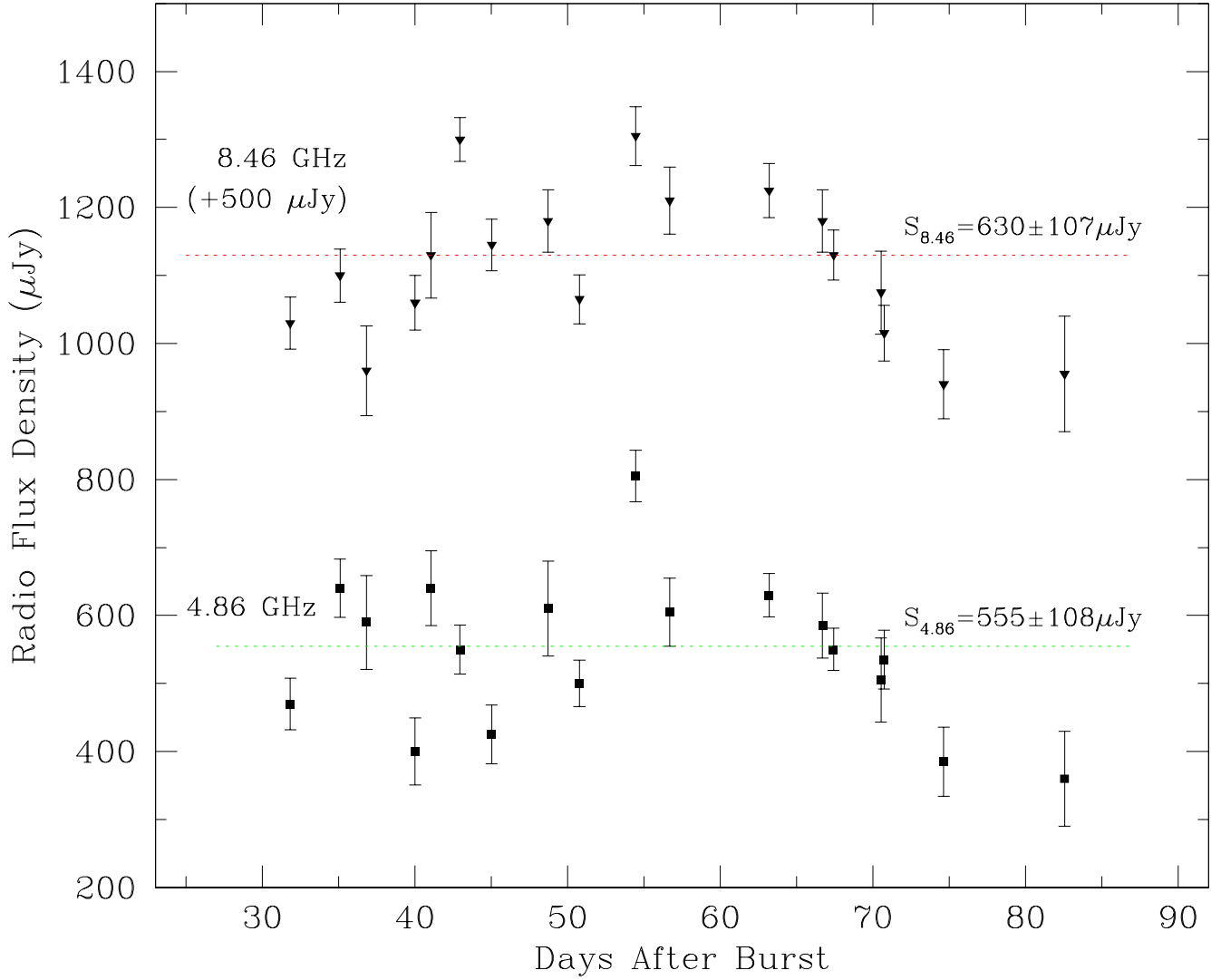


Fig. 2.— Radio light curves of GRB 970508 at 8.46 and 4.86 GHz in the interval between the the quenching of diffractive scintillation and the onset of the power-law decay. For ease of viewing, an offset of $500 \mu\text{Jy}$ has been added to the 8.46 GHz data. Flux densities indicated on the right hand side are the weighted mean and rms scatter of the data in this interval. In the text it is argued that the modest, broad-band variations are due to refractive scintillation.

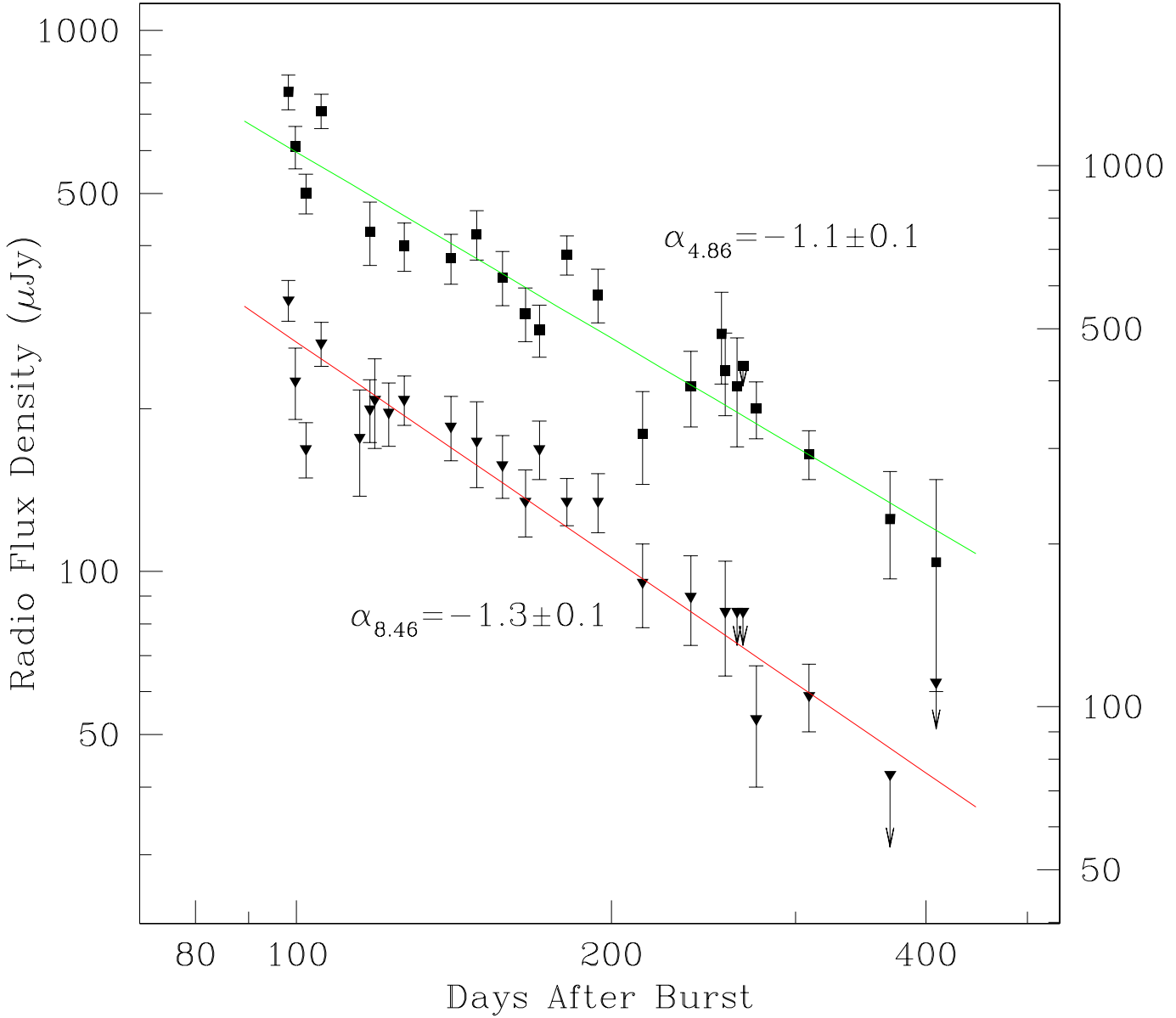


Fig. 3.— Radio light curves of GRB 970508 at 8.46 and 4.86 GHz in its decay phase. The left vertical axis is for 4.86 GHz, while the right vertical axis is for 8.46 GHz. Best-fit power law indices α are indicated by the straight lines.

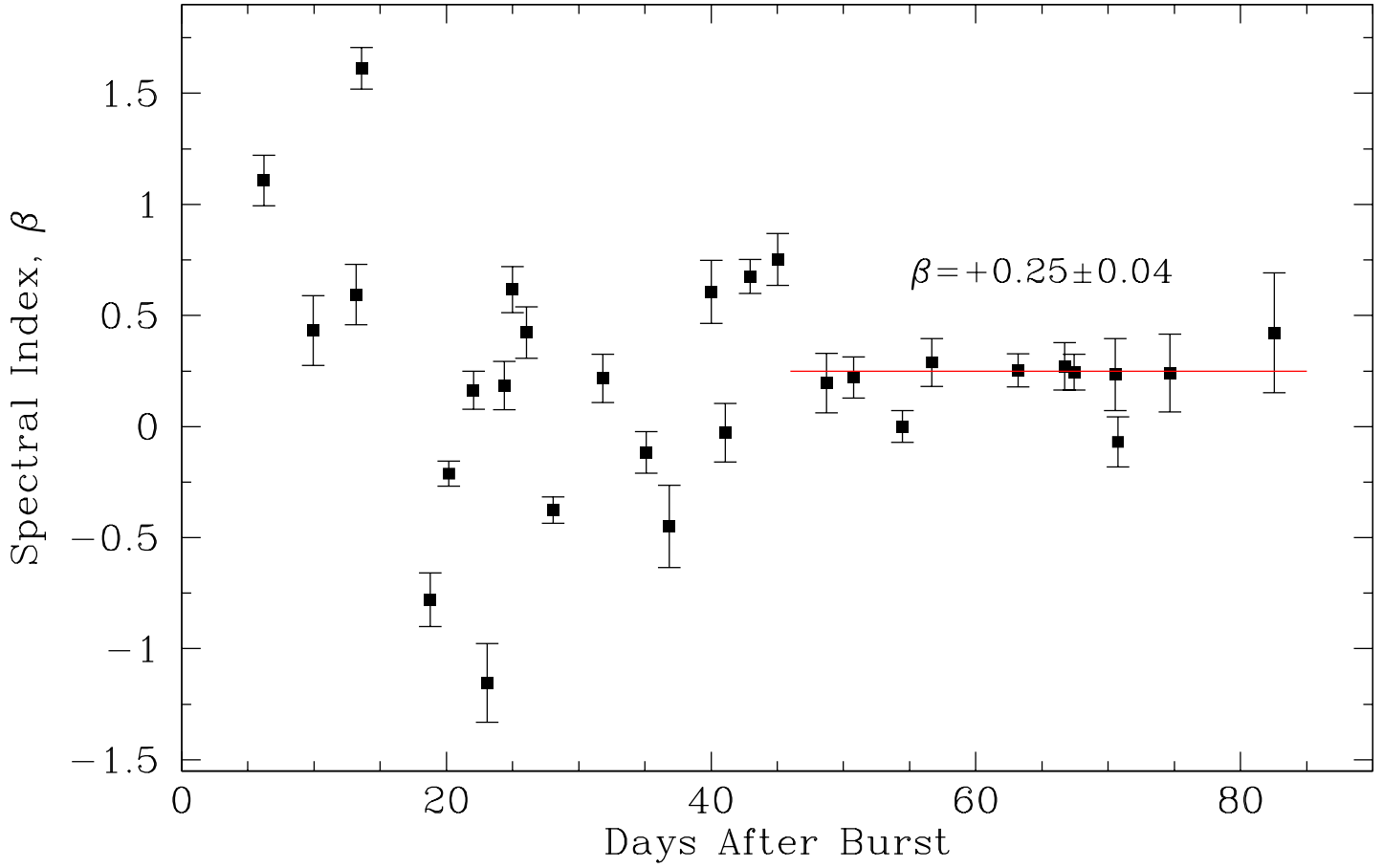


Fig. 4.— Spectral index plot between 4.86 GHz and 8.46 GHz showing quenching of the narrow-band diffractive scintillation and the emergence of the underlying low energy spectrum of the fireball. Values of β are plotted for all measurements in Table 2 for which simultaneous observations were made. The straight line is a weighted mean derived over the time range where it is drawn.

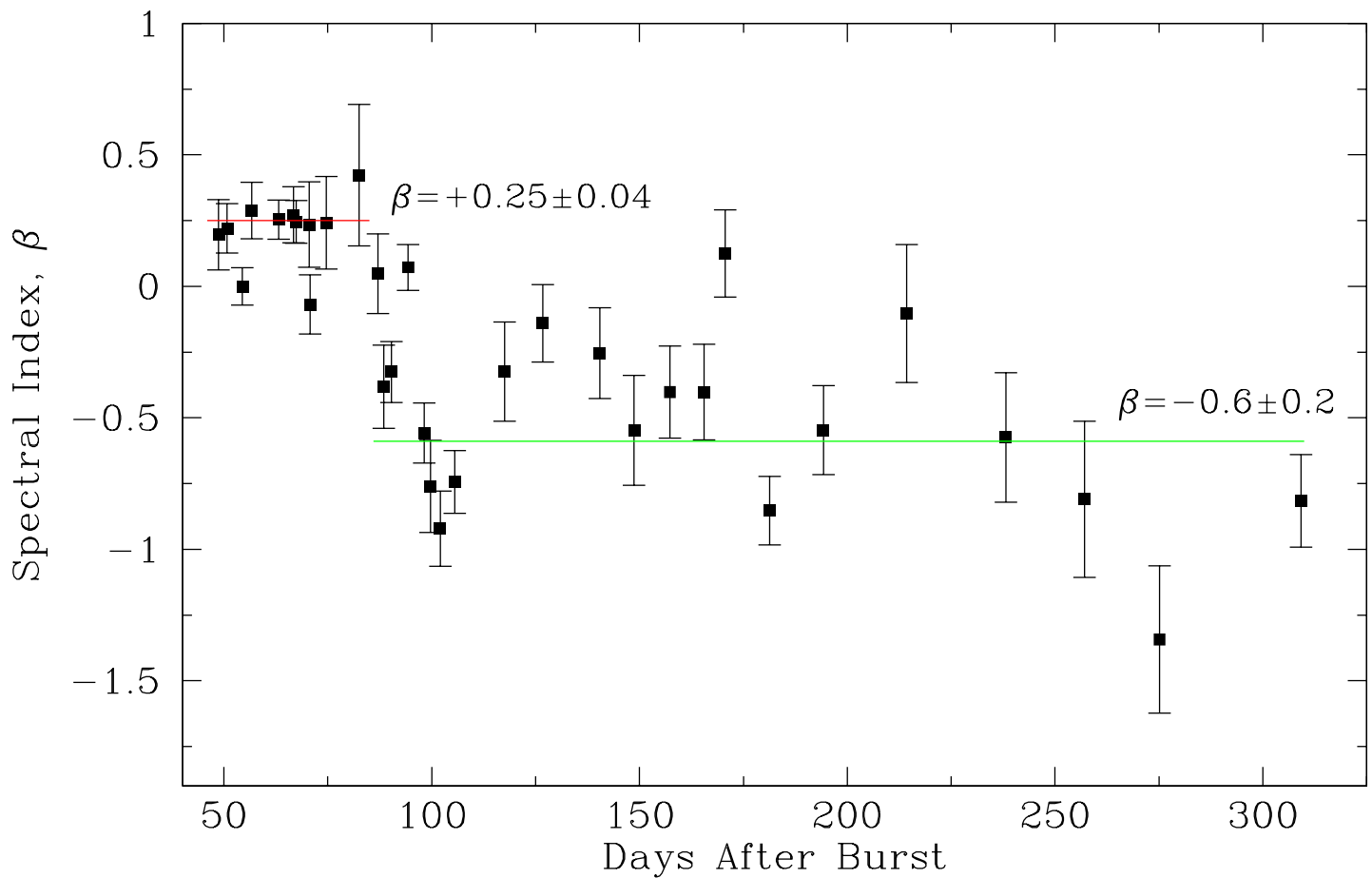


Fig. 5.— Spectral index plot between 4.86 GHz and 8.46 GHz. Values of β are plotted for all measurements in Table 2 for which simultaneous observations were made. The straight lines are weighted means derived over the time range where they are drawn.

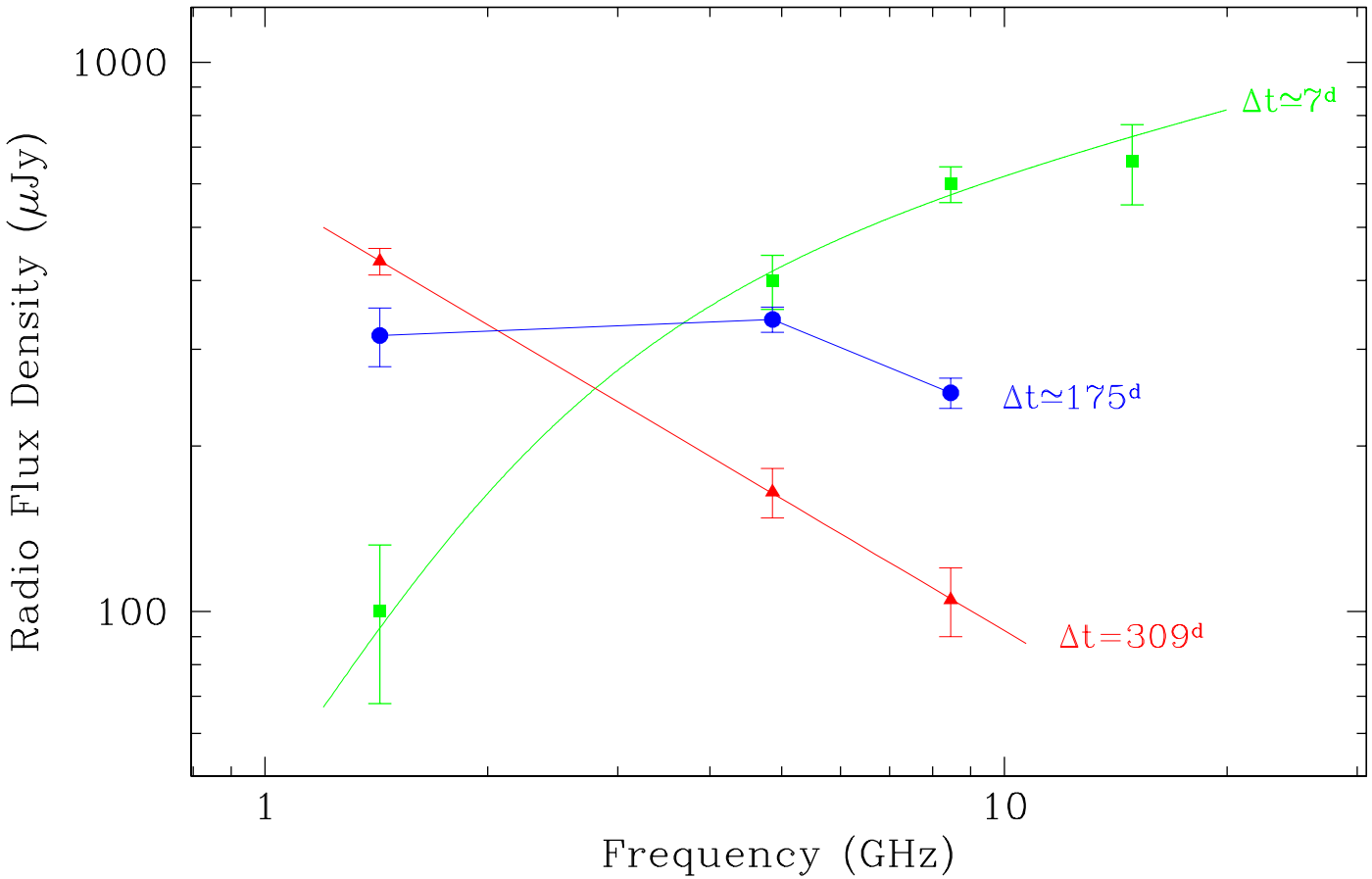


Fig. 6.— Spectral “snapshots” showing the evolution of the GRB 970508 in the radio band. The data points (solid squares) from day 7 are taken from Shepherd et al. (1998) and fit to the parameters derived by Granot et al. (1998). The data from near day 175 are averages taken around this time. The data at day 309 was taken just prior to the decay of the 1.43 GHz light curve and ar fit to a power law $\nu^{-0.8\pm0.1}$.

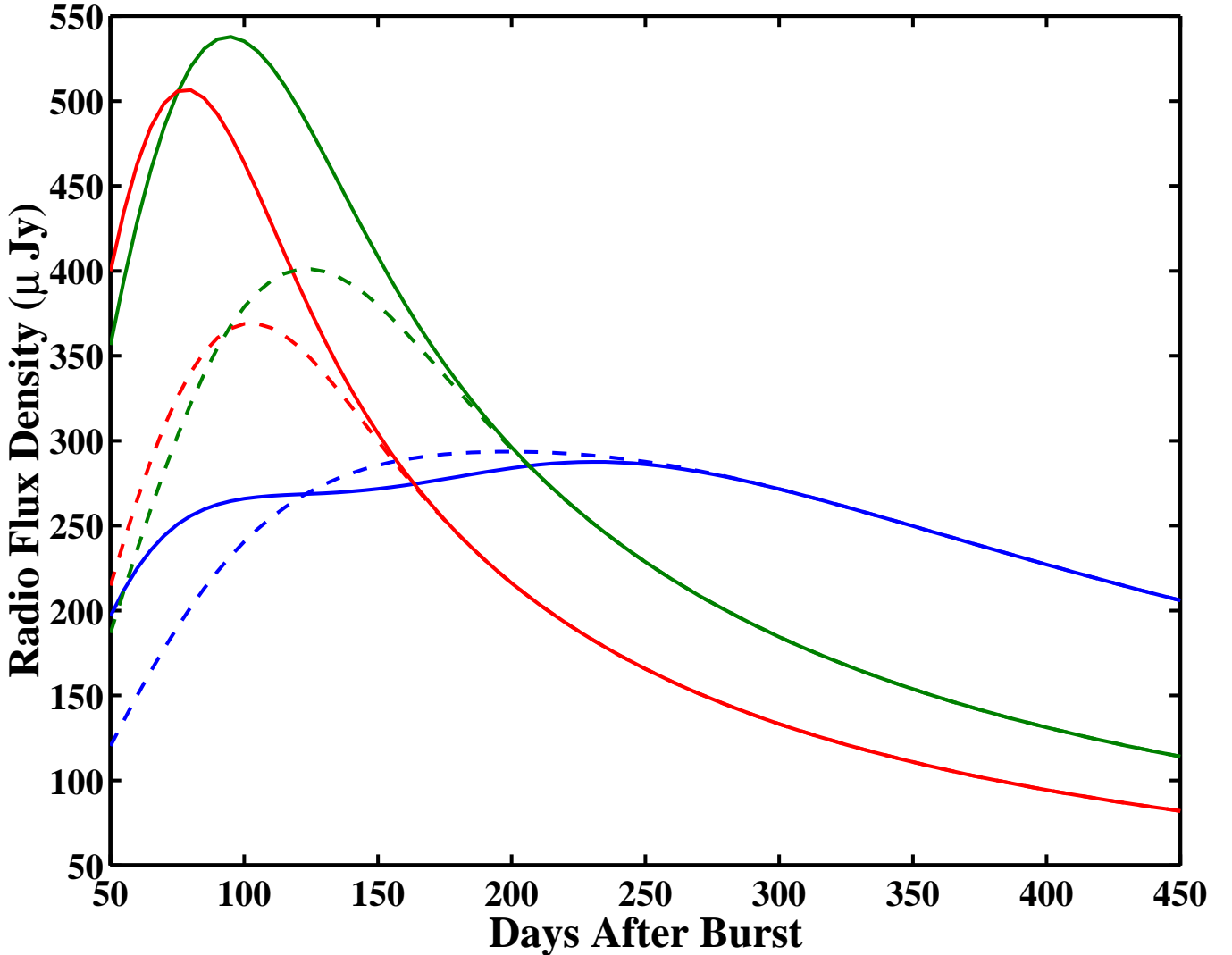


Fig. 7.— Model light curves for $a = 4.1 \times 10^{-51} \text{ g s}^{1/2}$, $b = 5.3 \times 10^{29} \text{ s}^{-3.1}$ and $\nu_0/(1+z) = 2.3 \text{ GHz}$ (solid curve), $\nu_0/(1+z) = 5.2 \text{ GHz}$ (dashed curve). Both models reproduce the normalization and power law time dependence of the 4.86 and 8.46 GHz fluxes (Figure 3), as well as the early time suppression of flux at 1.43 GHz. In both models the optical depth at 1.43 GHz initially increases, and then rapidly decreases as ν_{ab} drops below ν_m (cf. Eqs. A14, A17), allowing both models to correctly reproduce the approximately constant flux at 1.43 GHz at $t = 100 \text{ d}$ to $t = 300 \text{ d}$ (Figure 1). Both models also correctly predict the decrease of 1.43 GHz flux at $t > 300 \text{ d}$ (Figure 1).